SYNTHESIS AND CHARACTERIZATION OF CERIUM FLUORITES BASED ON $Ce_{1-x}Ln_xO_{2-\delta}$ SYSTEM (Ln: Nd^{3+}, Sm^{3+}, Eu^{3+}, Gd^{3+}, Dy^{3+} AND Ho^{3+})

JAIRO. A. GÓMEZ-CUASPUD[1]*

[1]*Universidad Pedagógica y Tecnológica de Colombia. Facultad de Ciencias. Grupo de Desarrollo y Aplicaciones de Nuevos Materiales DANUM. Av. Central del Norte 39-115, Tunja. Colombia.*

ABSTRACT

This paper describes the synthesis of 18 oxides of $Ce_{1-x}Ln_xO_2$ (Ln: Nd^{3+}, Sm^{3+}, Eu^{3+}, Gd^{3+}, Dy^{3+} and Ho^{3+}), with x = 0.05, 0.10 and 0.15 mol% by use of a wet chemical route that involving the obtention of coordination compounds type citrate, which allow the generation of a number of chemical and surface properties with potential catalytic applications in solid oxide fuel cells technologies. The materials obtained by this route, has a high purity and homogeneity, enabling calcination temperatures and residence times considerably brief, in comparison with conventional synthetic routes. All oxides, were calcined at 300 °C under flow oxygen and were characterized by X-ray diffraction (XRD), from obtained results, we confirmed the presence of a pure fluorite structure of CeO_2 consistent with the ICSD pattern reference of 072155 with space group *Fm-3m* (225). Subsequent physicochemical characterization by TPR and electron microscopy (SEM-TEM), confirm that cerium oxides could be reduced in two single steps at different temperatures, kinetically detectable and clearly prolonged as well as the obtention of nanostructured solids with a crystallite size between 32-47 nm. According with obtained results, the solids show a high surface area as result of the low calcination temperature. The electrical characterization by impedance spectroscopy (IS), revealed an important concentration of charge carriers in fluorite oxides, mainly in the sample of GDC5, which is a crucial characteristic in advanced materials for SOFC applications. The catalytic studies, conducted on materials at 700 °C under stable reaction conditions, confirm that the methane conversion levels change throughout the series GDC5 → NDC5 → HDC5 → EDC5 → DDC5 → SDC5, which established that the GDC5 solid, exhibits the most promising results. Finally, a stability test was achieved with the GDC5 catalyst under the same reaction conditions established in previous form, for a period of 240 hours of continuous flux, establishing the effectiveness of the proposed method to choice the most promissory material. The results confirmed as the methane conversion vary as function of time and the obtained syngas levels change for potential technological applications.

Keywords: Fluorite, Impedance, Polymerization, TPB.

1. INTRODUCTION

During last decades, an increasing and continuous interest for fuel cells and use of hydrogen as fuel in new devices has emerged as one of the most highlighted alternatives for energy production in several and critical sectors of an economy based on the consumption of fossil fuels [1, 2]. A fuel cell is an energy conversion device, similar to an electrochemical cell, but designed for continuous feeding, producing electricity from an external fuel and oxygen source in contrast with limited storage capacity of a battery. Advantages of this class of fuel cells include high efficiency, long-term stability, fuel flexibility, low emissions, and relatively low cost [3]. Between the large number of devices that can be classified according to their operating temperature and the nature of the type of electrolyte, are the called solid oxide fuel cells (SOFC´s), which have the highest operating temperature (500-1000 ºC) and a ease in the fuel processing. At these temperatures, SOFC devices do not require expensive platinum catalysts, as is currently necessary for lower-temperature fuel cells such as Polymer Electrolyte Membrane Fuel Cells (PEMFC´s), and are not vulnerable to carbon monoxide poisoning. However, vulnerability to sulfur poisoning as has been widely observed and the sulfur must be removed before entering the cell through the use of activated charcoal and some alkaline materials. Hence, the SOFC´s offer a promising alternative to obtention of clean energy and enable the use of in situ process as steam reforming as hydrogen source [3]. Based on previous advantages, diverse enhancements in components of these devices have been suggested, mainly in the field of anodes, since they are responsible for oxidation reaction between the fuel and the oxygen ions (O^{2-}), moreover to facilitate the move of electrons produced in this reaction and transport it to external path without electrical loss [4]. Therefore interest has focused on the use of alternative materials for anodes such as perovskites [5], fluorites [6], ruthenium oxides [7] and pyrochlores [8]. Among others, the cerium oxides derived from fluorite structure type and modified with transition elements, are one of the most promissory materials that have reduced the sulphur poisoning and have improved the electrical performance, with high levels of reliability, stability, conductivity, resistance to carbon deposition and good catalytic properties on steam methane reforming [9]. Although, several studies confirm that anodic oxides type fluorite are rapidly sintered under SOFC reaction conditions with an important loss of most of surface properties, incorporation of some transitional cation metals along lanthanide series may resolve these negative effects.

Since catalytic efficiency is one of the most important aspects in development of new anodic materials for SOFC devices, the use new synthesis routes represent an imperious requirement in development of new promissory materials. Thus, some metal oxides with fluorite structure have been investigated as one of the most important catalysts for eventual applications. Menon *et al*. [10] has reported a lot of information about the behavior of the different catalysts for application in anodic components for SOFC devices, showing that is necessary to promote the direct steam reforming to supply hydrogen without use of external reformers, mainly concentrated in a geometrical zone where anodic catalyst can be in contact with a gas phase of fuel and the electrolyte, such active zone so-called triphasic boundary (TPB), is a parameter of crucial importance for the performance of SOFC systems. In general a wide TPB is required for a high electrochemical performance, allowing the movement of a larger number of charged species during a chemical reaction improving the reactivity levels. In this regard, the use of different fluorites based on $Ce_{1-x}Ln_xO_{2-\delta}$ system could modify the activity and selectivity to hydrogen production on the steam methane reforming reaction, with aim to identify some important aspects of process [11-15].

Therefore, this research focused on the synthesis and characterization of 18 $Ce_{1-x}Ln_xO_{2-\delta}$ oxides (Ln: Nd^{3+}, Sm^{3+}, Eu^{3+}, Gd^{3+}, Dy^{3+} and Ho^{3+}), with x = 0.05, 0.10 and 0.15 mol% by a wet chemical route based on polymerization-combustion process with the aim to study the effect on structural, morphological, electrical and catalytic properties of the modified fluorites for use as potential anodic components in SOFC devices.

2. EXPERIMENTAL

2.1 Preparation of fluorites

Active phases of $Ce_{1-x}Ln_xO_{2-\delta}$ (Ln: Nd^{3+}, Sm^{3+}, Eu^{3+}, Gd^{3+}, Dy^{3+} and Ho^{3+}), with x = 0.05, 0.10 and 0.15 mol% were prepared by polymerization-combustion technique, starting from corresponding nitrates of $Ce(NO_3)_3.6H_2O$ (99.9%), and $Ln(NO_3)_3.9H_2O$ 99.99% nitrates with citric acid monohydrated (99.99%). Stoichiometric quantities of each solid (1:1) salt were added to 20 mL of absolute ethanol, as reported in previous literature [16]. Once reached a total dissolution of each nitrate solutions, the solid citric acid was added at 0.5:1 molar ratio with respect to the total concentration of metal cations in dissolution. The 18 solutions were kept under reflux at 120 °C for 12 hours

e-mail: jairo.gomez01@uptc.edu.co

until formation of a viscous liquid, which was then heated at 150 °C under air flux in an oven until complete solvent evaporation and treated at 250 ºC to initiate the combustion process. The carbonaceous remnant was removed by thermal treatment at 300 °C under oxygen flow for 3 hours. The samples were kept in a chamber under controlled humidity (20 %) before catalytic tests [16].

2.2 Characterization of catalysts

The chemical composition of all samples was obtained using X-ray fluorescence (XRF) technique, using an apparatus Philips MagiX Pro. Samples were pressed at 5 Mpa and analyzed quantitatively. The specific area BET was evaluated by nitrogen adsorption isotherms at -196 ºC, using the ASAP-2020 apparatus (Micromeritics), degassing at 350 ºC overnight to remove residual humidity.

The crystalline structure was determined by X-ray diffraction, in a PANalytical X'Pert PRO MPD equipment, using Cu K_α radiation (λ = 1.54186 Å) between 10° and 90°, with steps of 0.05°. Refinement, indexing and the simulation of the structures were done with MAUD software that allowed us to establish the chemical composition and crystallographic structure of the obtained oxides. The crystallite sizes were calculated using the highest diffraction signals, using the Debye-Scherrer equation, taking the value of half peak width set by a Lorentzian function and using a constant of 0.89 as reference.

Temperature programmed reduction (TPR-H_2), was performed in a Chembet 300 (Quantachrome) equipment. The samples were heated at 200 ºC for 2 h, flowing pure helium and then reduced with a mixture of 5% H_2/He (30 mL min^{-1}), rising up to the maximum temperature reduction at 10 ºC min^{-1}. The H_2 consumption was measured using a thermal conductivity detector.

Transmission electron microscopy analysis (TEM) were performed on a JEOL 2100 equipment using a LaB_6 thermionic gun operated with an acceleration voltage of 200 kV, equipped with a CCD imaging system. For analysis, these samples were ground to obtain fine powders, which were sieved to 200 U.S. standard mesh and dispersed in a test tube with 5.0 mL of water and each tube was placed in a ultrasonic equipment for 30 min, after which a drop of the top of each tube was taken and dried at 45 °C for respective analysis.

2.3 Catalytic test

The samples were tested on the steam methane reforming reaction. The reaction was performed in an experimental unit consisting of a set of mass flow meters (MKS) and a reactor coupled to a resistive furnace. A reaction mixture (CH_4/H_2O/Ar), was used with a flow of 8/24/68 mL min^{-1} respectively, which was pre-heated at 200ºC before catalyst contact in a U shape quartz micro-reactor with 12 mm ID and 250 mm long at 700 °C. The oxides were supported over quartz wool.

The oxides were dried at 300 °C for 30 min prior catalytic tests under helium flow (30 mL min^{-1}). After cleaning and cooling, the gas valve was switched to the gas mixture and adjusted until stabilization, GHSV = 18000 h^{-1} and a contact time of 0.20 seconds. The reaction was studied under isothermal condition at 700 °C, exhaust gases were analyzed by gas chromatography (HP 5890 series II) equipped with a packed column HAYESEP Q of 5.5 m long, ¼" pore diameter and an inner diameter of 80/100 and a TCD detector. Finally, the FID flame detector allow evaluate the formation of minor species, the selectivity (S_{CO}, S_{H2}) and the most important products derived from steam methane reaction.

Main products from catalytic reaction were hydrogen, methane, carbon dioxide and carbon monoxide. The conversion of methane was calculated from carbon products in molar balance (on dry basis), presented in Eq. 2 where γ_{Ci} is the ratio of carbon content of product ***i*** to carbon content of methane molecule, and $\boldsymbol{y}_{Ci}$ is the molar fraction of carbon content products in the effluent flow. The molar selectivity was defined as the ratio of moles of one product and the total moles of products, based on experimental values.

$$X_{Methane}(\%) = \frac{\Sigma\ \gamma_{Ci}\ y_{Ci}}{y_{Methane} + \Sigma\ \gamma_{Ci}\ y_{Ci}} \times 100 \qquad (2)$$

Finally, in order to provide useful information on physicochemical properties of the materials, impedance spectroscopy analyses were performed, allowing to evaluate the electrical properties of solids and the microscopic characteristics of crystallites by variable frequency data, which was obtained by an impedance analyzer Agilent 4294A between 40 Hz to 13 MHz with an ac amplitude of 0.1 volts. For fixed-frequency measurement in the selected range, we used a QuadTech 1920 LCR Analyzer, obtaining Nyquist type impedance plots. For this purpose, it was prepared several pellets of 0.060g of finely ground solids, using isostatic pressure (vacuum) of 1.0 Mpa, in a Perkin-Elmer system for 60 seconds. Obtained tablets were polished using SiC abrasive paper 1200, in order to provide a uniform contact surface, adjusting the thickness of the pellet at 0.50 mm. Data derived from this analysis were corrected by the global geometry of the tablet and the reference cell using the Z-plot software.

3. RESULTS AND DISCUSSION

3.1 Catalyst Preparation and Characterization

The chemical compositions of all samples were calculated by X-ray fluorescence, as presented in Table 1. These results are close to the proposed nominal values and permit to evaluate the control in stoichiometry of ceramics. In general, a comparison between different modification levels along of the suggested compositions yielded good accuracy percentages.

Table 1: Elemental composition of $Ce_{1-x}Ln_xO_2$ oxides derived from X-ray fluorescence analysis.

Lanthanide modification by system (0.05, 0.10 and 0.15 mol %)	Sample identification	Obtained composition (%)
$Ce_{1-x}Nd_xO_2$	NDC5	4.48
	NDC10	9.36
	NDC15	14.52
$Ce_{1-x}Sm_xO_2$	SDC5	4.35
	SDC10	9.68
	SDC15	14.98
$Ce_{1-x}Eu_xO_2$	EDC5	4.79
	EDC10	9.76
	EDC15	14.10
$Ce_{1-x}Gd_xO_2$	GDC5	4.84
	GDC10	9.64
	GDC15	14.50
$Ce_{1-x}Dy_xO_2$	DDC5	4.89
	DDC10	9.82
	DDC15	14.98
$Ce_{1-x}Ho_xO_2$	HDC5	4.85
	HDC10	9.94
	HDC15	14.76

The specific surface areas of the pure oxides (S_{BET}, $m^2\ g^{-1}$), are presented in Table 2, using the same mass per test. Results show that the initial surface area is relatively high, in comparison with the same fluorite type oxides obtained by other techniques such as solid state reaction or ball milling [17], so, is clear that the synthesized materials under present chemical conditions, shown similar specific areas influenced by the development of nanometric solids with potential catalytic properties. Although, the surface area of the $Ce_{1-x}Ln_xO_2$ samples can be attributed mainly to the reduced thermal treatment in the synthesis process, the preservation of textural and morphological characteristics depends besides of the use and choosing of appropriate chelating agents and of the exhaustive control on aqueous conditions between others, which promotes the generation of compounds with a high purity level and homogeneity [18].

The XRD patterns of $Ce_{1-x}Ln_xO_2$ oxides after combustion and calcination processes are shown in Figs. 1 and 2, for different compositions and percentage modifications. Following the development of XRD patterns, not is possible notice the influence of lanthanide modification, along of cerium oxides as shown in Fig 1, in which a very defined fluorite phase could be observed, whose main signal was centered at (1 1 1) facet, become easily indexed. Results analyzed by X´pert High Score software confirm the presence of a single phase of CeO_2 oxide (ICSD: 072155), with space group *Fm-3m* (225) in accordance with previous literature [19]. The 18 experiments have led to well crystallized nanostructures with crystallinity above 95%, evaluated from the internal standard method, in a *FCC* system with lattice parameters of 5.35 ± 0.003 Å in all cases without detectable variations. All powders displayed crystallite sizes inferior to 50 nm according to Scherrer's equation taking a value of half peak width (β), adjusted to a Lorentzian function and using a constant of 0.89 as

reference, indicating the presence of nanometric crystallites in all cases, which contributes little to the catalytic activity of solids, as shown in Table 2 [16].

Table 2: Surface area of modified $Ce_{1-x}Nd_xO_2$ oxides.

System	Sample identification	Surface area (m^2/g)	Crystallite size (nm)
$Ce_{1-x}Nd_xO_2$	NDC5	15.5	40
	NDC10	16.1	38
	NDC15	16.5	35
$Ce_{1-x}Sm_xO_2$	SDC5	14.9	39
	SDC10	16.0	40
	SDC15	16.1	41
$Ce_{1-x}Eu_xO_2$	EDC5	17.6	44
	EDC10	17.7	45
	EDC15	17.9	45
$Ce_{1-x}Gd_xO_2$	GDC5	17.3	33
	GDC10	17.8	35
	GDC15	18.5	38
$Ce_{1-x}Dy_xO_2$	DDC5	17.0	42
	DDC10	17.1	43
	DDC15	17.8	45
$Ce_{1-x}Ho_xO_2$	HDC5	16.4	41
	HDC10	16.5	44
	HDC15	16.6	46

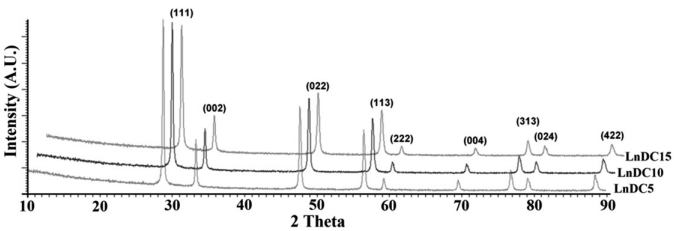

Fig. 1 XRD patterns of cerium oxides with different internal transition element modification level.

From results showed in Figure 2, is clear that effect of lanthanide cation with compositions of 5% molar concentration has no influence on fluorite structure, which shows that solid solutions of cerium oxide, exhibit a single crystallographic phase. At this level the lanthanide content is not enough to modify the crystallographic parameters, only until 50 % molar concentrations the presence of Ln^{3+} in cerium oxides could affect the structure and be detectable by X-ray diffraction [20]. Furthermore, since no detectable changes were observed, the formation of impurities can be discarded.

The TPR-H_2 profiles of $Ce_{1-x}Ln_xO_2$ oxides are shown in Fig. 3. The maximum reduction signal of reference cerium oxide occurred under progressive signals at 560 and 850 °C, corresponding with reduction of CeO_2 and Ce_2O_3 oxides respectively. According to Jacobs *et. al.* [15], the reduction analysis with hydrogen, confirm that cerium oxides could be reduced in two single steps at different temperatures, kinetically detectable and clearly prolonged as shown in Eqs 2 and 3. For NDC5, NDC10 and NDC15 systems, behavior is wide different, since presence of neodymium cation in cerium oxide structure promotes an early reduction of Ce^{4+} to Ce^{+3} signal at low temperatures, due to increment in concentration of lanthanide cation in fluorite structure as occur in other oxides. This behavior is extended kinetically to high temperature signals (Ce^{3+} to Ce^0), which are affected progressively from 850, 757, 730 and 702 °C allowing evaluate the concentration effect along a modified series of fluorites.

$$2CeO_2 + H_2 \rightarrow Ce_2O_3 + H_2O \quad (2)$$
$$Ce_2O_3 + 6H_2 \rightarrow 2Ce^0 + 3H_2O \quad (3)$$

Figure 4 shows the smoothed profiles and restored RTP-H_2 signals for all synthesized fluorite oxides, detecting the most significant signals of each series. These results suggest the presence of a single reduced specie, corresponding with the major compound of Ce_2O_3. It is also clear that the reduction temperature along of the worked lanthanide series, is variable and is associated with the nature of the modifying cation, in this way, there is a small increase in the reduction temperature in the sequence NDC5 → EDC5 → HDC5 → SDC5 → GDC5 → DDC5, of which, the GDC5 and DDC5 samples are reduced at temperatures above 830 °C, showing a greater degree of stability to the reducing atmospheres, possibly stimulated by the presence of a single and stable valence (3+) [15, 21]. By other hand, EDC5 and SDC5 samples are reduced at temperatures below 800 °C, exhibiting two oxidation states (2+ and 3+), situation which promotes a different behavior. It is also interesting to see how the NDC5 sample, which has a single oxidation state (3+), show the lowest reduction temperature of the studied series, the condition is justified by the neodymium reduction potential, which is capable of altering the redox stability of the modified fluorite in almost 100 °C. Thus, it is clear that DDC5 and GDC5 samples are materials that offer the greatest benefits in terms of the redox stability, while the NDC5, SDC5 and EDC5 oxides not provide any advantage for eventual applications on design of SOFC anodes.

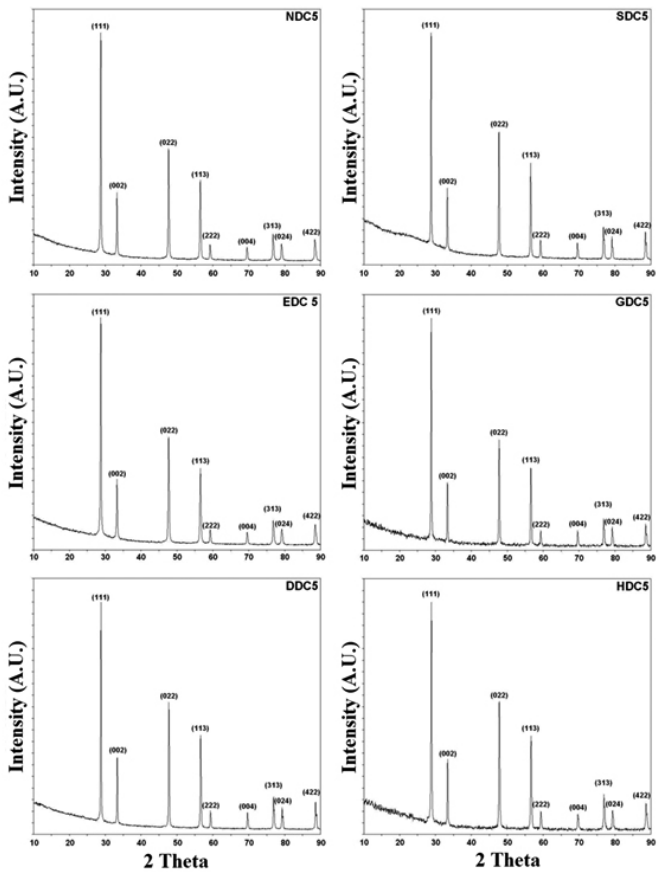

Fig. 2 XRD patterns of $Ce_{1-x}Ln_xO_{2\ \text{oxides with different transition}}$ elements at the same modification level.

At microscopic level, the solids are composed by irregular aggregates with sizes between 0.5 to 150 mm for all samples with a slight agglomeration effect, in which there is no difference between materials with variable degrees of modification, nor there significant changes in the sequence of lanthanide series. These results provide evidence about the process in the formation of larger aggregates which grown and form irregular particles, due to low surface energy associated to formation of these oxides during combustion process. These pictures are related with the texture and the relief formed by elimination of solvent during evaporation and combustion of organic compounds after thermal treatments as has been reported in previous literature [16]. The SEM micrographs confirm that densities of all samples have a considerable fraction of open and closed porosity located both between and within the grains. On the basis of these results it is obvious that synthesis method, promotes some degree of densification, as well as, formation of heterogeneous grained microstructures as shown in Fig.5.

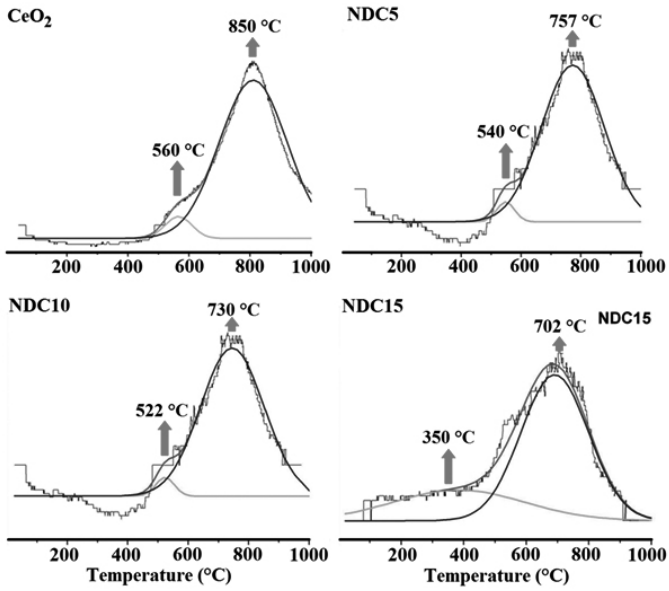

Fig. 3 TPR-H_2 profiles for reference CeO_2 oxide and $Ce_{1-x}Nd_xO_2$ series with different modification level.

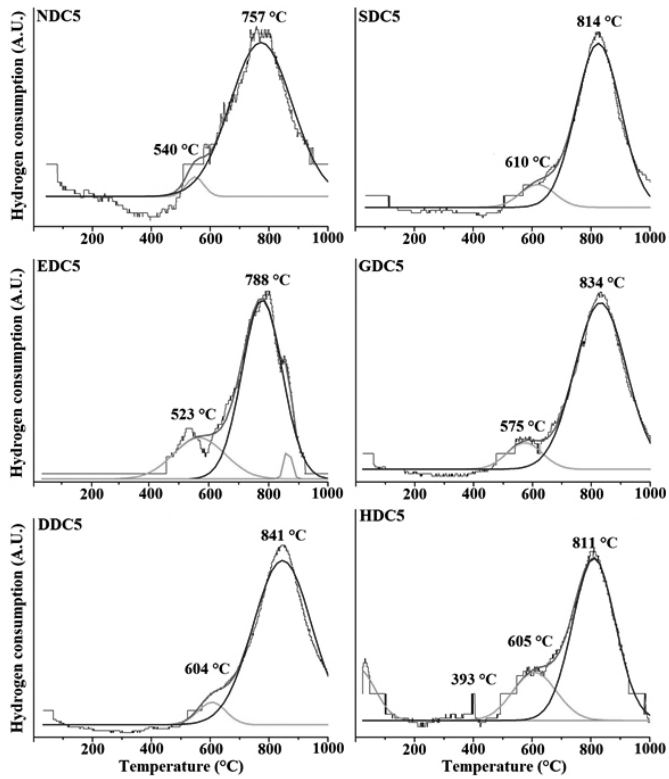

Fig. 4 Smoothed TPR-H_2 profiles and deconvoluted signals for $Ce_{0.95}Ln_{0.05}O_2$ fluorites (Ln = Nd, Sm, Eu, Gd, Dy and Ho).

From results derived on Fig. 6., is clear that oxides suffered some degree of densification as a function of thermal treatment used for calcination process, fact that favored the appearance of a compact morphology that although was reflected in the intensity of the reflections in the (1 1 1) facet, not affect significantly the crystallite size.

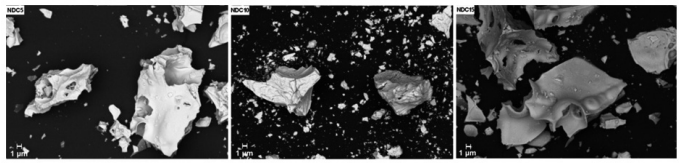

Fig. 5 Scanning electron micrographs for $Ce_{1-x}Nd_xO_2$ samples modified with 0.05, 0.10 and 0.15 mol% respectively.

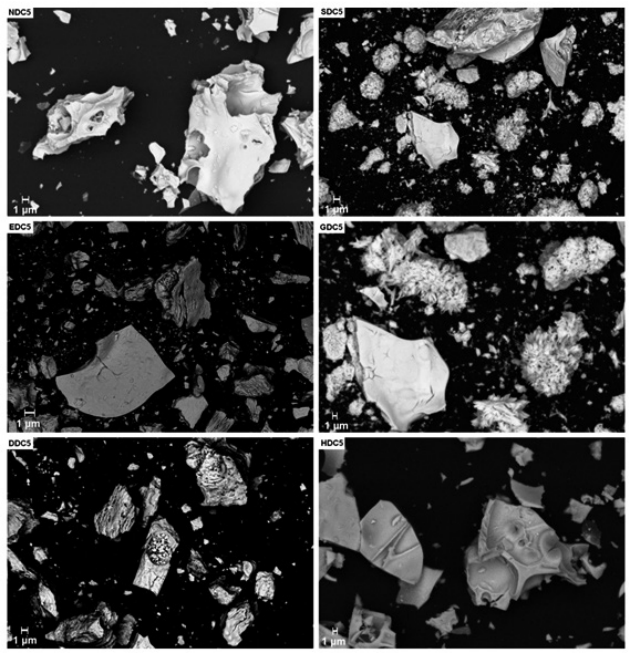

Fig. 6 Scanning electron micrographs for $Ce_{0.95}Ln_{0.05}O_2$ samples with Ln = Nd, Sm, Eu, Gd, Dy and Ho.

The TEM images of neodymium doped ceria oxides annealed at 300 °C, indicate the obtention of solids with a narrow size distribution consistent with nanosized particles, the data derived from checking the lattice parameters of more than 50 images of this sample were evaluated by the ELMIX software, in which, the obtained particles of an average diameter of 25 nm tend to form octahedral crystals with the (1 1 1) facet exposed and display a calculated grain boundaries of about 1 nm as shown in Figure 7.

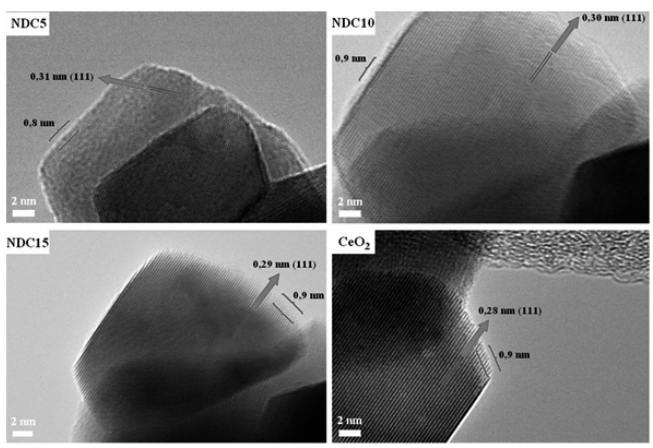

Fig. 7 TEM micrographs of $Ce_{1-x}Nd_xO_2$ samples modified with 0.05, 0.10 and 0.15 mol% respectively with obtained d-spacings and grain boundary widths.

The results from statistical counting in all micrographs for the 18 samples obtained, in a population of 150 particles, were recollected and normalized to

obtain a regular distribution of crystallite sizes with characteristic morphology and respective calculated *d*-spaces, which ratify previous analyses, derived from X-ray diffraction and confirm the potential catalytic applications of the materials. Similarly, there is no evidence of important linear and surface defects, such results are closely related with X-ray diffraction analysis in which the structure of a face-centered cubic fluorite (*FCC*) was conserved along of the modified series and only a slight contraction of *d*-spacing was evidenced in Nd → Sm → Eu → Gd → Dy → Ho sequence according to [21], as shown in Fig. 8.

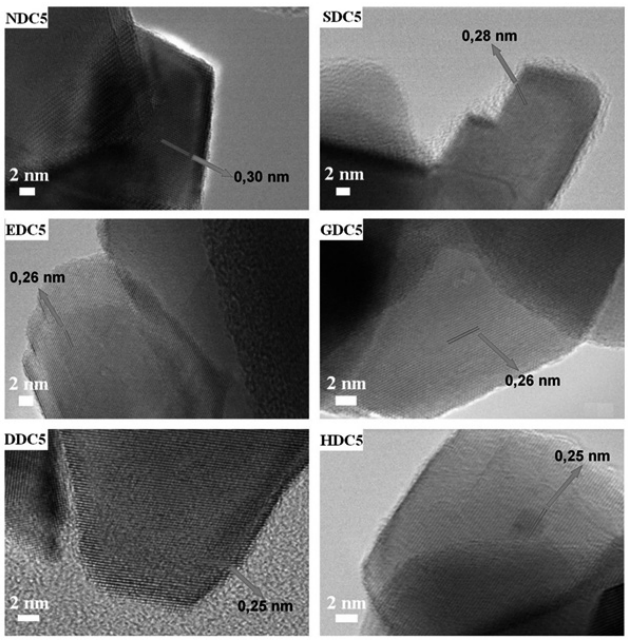

Fig. 8 Transmission electron micrographs for $Ce_{1-x}Ln_xO_2$ samples modified with 0.05 mol% and its corresponding and calculated d-spaces.

Figure 9 displays the histogram of particle size distribution for all obtained oxides, showing a single modal distribution with a marked Gaussian behavior, revealing the presence of nanometric particles homogeneously distributed from 32 to 47 nm due to the low calcination temperature after combustion process. The chemical homogeneity and purity of all samples was tested by energy dispersive of X-rays analysis (EDX), indicating a homogeneous composition profile throughout the volume of solids, result previously confirmed by XRF analysis.

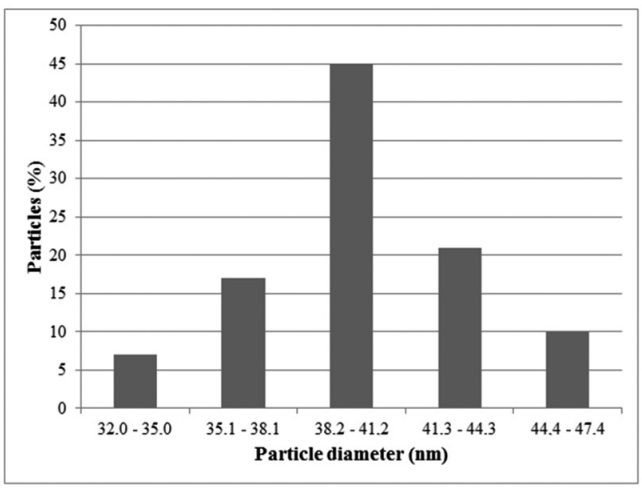

Fig. 9 Particle size distribution estimated from transmission electron microscopy data for obtained samples of $Ce_{1-x}Ln_xO_2$.

With base on preliminary data, is clear that the samples identified as DDC5 and GDC5, are materials that offer the greatest benefits in terms of the redox stability, surface area and the crystallite size, due to presence of a single oxidation state, that produce a decreasing lattice energy of the system and allows the establishment of more stable oxide structure with a high catalytic activity for SOFC applications [21]. Thus, the cerium oxides samples were tested by means impedance spectroscopy with the purpose of evaluate the properties of the solids to enable charge transfer under a steady state and isothermal conditions on steam methane reforming reaction.

3.2 Analysis by impedance spectroscopy (IS)

In order to determine the electrical properties of materials, impedance data were measured at 600 ºC and 800 °C. The data were collected for all samples and a reference cell, results were plotted in terms of the complex impedance (Z_{im}) and the real impedance (Z), to confirm that oxides has a conductor behavior, whose total RC resistance is strongly associated with the resistivity of grain according to McIntosh, *et. al*. [22]. Obtained results are consistent with a semiconducting behavior, since the solids are composed of transition elements that promote the ability of movement of charge carriers. It is also certain that the geometry of the semicircles signals does not correspond to a completely regular one, where the corresponding adjustment and smoothing practiced by the Zplot software, indicate a high degree of correlation in which the frequency (ω) and relaxation time can be determined from the signal of each semicircle, where ω*t* is equal to 1 as shown in Fig. 10 and Table 3.

Fig. 10 Nyquist impedance plots with ωτ time constant representing the electrical behavior of the system $Ce_{0.95}Ln_{0.05}O_2$, (Ln = Nd, Sm, Eu, Gd, Dy and Ho).

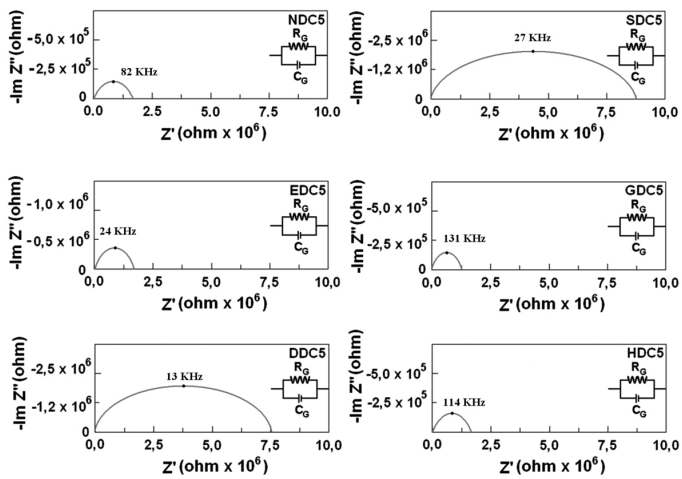

Table 3: Comparison between frequency, resistance, capacitance and conductivity values obtained at 25 °C for $Ce_{0.95}Ln_{0.05}O_2$, (Ln = Nd, Sm, Eu, Gd, Dy and Ho) samples, derived from Zplot software.

System	Frequency (Hz) x 10^4	Resistance (ohm) x 10^6	Capacitance (Farads) x 10^{-12}	Conductivity ($ohms^{-1}cm^{-1}$) x 10^{-7}
NDC5	8.22	1.64	6.02	6.09
SDC5	2.71	8.90	3.75	1.12
EDC5	2.49	2.36	13.5	4.23
GDC5	13.1	1.32	4.98	7.57
DDC5	1.34	6.41	9.02	1.56
HDC5	11.4	1.66	4.64	6.02

The impedance plots show one semicircular arc with its center lying below the real axis of impedance. The presence of a unique semicircle confirms that the polarization mechanism in cerium oxides corresponds with a bulk effect, arising in limits of semi-conductive grains. This result provides an insight into the electrical processes occurring in materials, characterized by a small capacitance of the materials which vary between 3.75 x 10^{-12} to 13.5 x 10^{-12} Farads in concordance with previous works [23]. The conductivities of the cerium oxides show different values, with Nd, Gd and Ho as the materials with the highest values. The maximum conductivity observed was 7.57 × 10^{-7} S cm^{-1} for GDC5 sample in contrast with the SDC5 and DDC5 samples, in which conductivity values reach 1.12 × 10^{-7} and 1.56 × 10^{-7} S cm^{-1} respectively.

The conductivity of doped ceria oxides vary substantially along substitution series of rare earth oxides as shown in Table 3 and Fig.10. The maximum conductivity, was observed for the compositions in which the substituting cation exhibit a unique oxidation state. Although the conductivity generally increases in a direct form with the ionic radius of the dopant cation, no correlation was found between these two variables. For several of these materials, the relative contribution of the bulk crystal lattice and grain boundaries to the overall resistance was measured, the relative significance of each one depend on the type of rare earth dopant and the processing condition according to Göbel and Anjaneya [23, 24].

The microstructural characterization of solids using ac impedance confirms that the modification with rare earth oxide dopants on cerium oxide structure, promotes changes in the crystal lattice and ionic conductivity. With increasing dopant radius, the lattice parameter of the ceria unit cell increases in a fairly regular way. In all cases cation modification increases the concentration of oxygen vacancies, which results in a growth of ionic conductivity according to Gao [25]. In agreement with previous works [26-29], the Nd, Gd and Ho modified oxides, yielded the highest conductivities although no exist an exact correlation between ionic radius and conductivity.

It is apparent that the distinction between grain boundary and grain interior resistance is a very important fact. Our results indicate that processing and synthesis conditions, can play an important role in this issue. One derived conclusion from this results, is related with fact that contribution of the grain boundaries to the total resistance could be minimized by implementation of a more effective synthesis route like the combustion process that permit to obtain solids with a high purity and homogeneity level, whereby properties as ionic conductivity could be significantly improved [23, 25]. Because of its higher conductivity, the gadolinium doped ceria appears to be a promising solid electrolyte to be used in solid oxide fuel cells, thus with the purpose of clarify this aspect, a catalytic study on steam methane reforming was developed in an effort to validate the proposed analysis process of the synthesized samples, with aim to predict the catalytic behavior of materials under eventual operating conditions of SOFC devices.

3.3 Activity and selectivity

The temperature of steam methane reforming reaction was kept at 700 ºC using a gas hour space velocity (GHSV) = 18000 h^{-1} with a contact time of 0.20 seconds for all experiments over a period of 6 hours. The catalytic test was carried out over powdered samples of cerium oxides, the results are shown in Table 4, in which is clear that reactivity and selectivity towards preferred products as carbon monoxide and hydrogen steam methane conversion varying in at least 14.1% ± 0.5 from most active phase of GDC5 to less active of SDC5, confirming previous results of impedance measurements in which is clear that development of chemical reactions as steam methane reforming are strongly controlled by charge transfer processes in the vicinity of the TPB, enabling that methane conversion take place along GDC5 → NDC5 → HDC5 → EDC5 → DDC5 → SDC5 series, in the same form as electrical conductivity values showed in Table 3 [30]. The CO and H_2 selectivity for GDC5 sample, confirm that average values of steam methane conversion of about 69.20%, correspond with the obtention of 69.30 H_2 and 67.45% for CO, values normally accepted for supported nickel catalysts [31-32]. Similarly, the catalytic reactivity expression in terms of methane conversion ($X_{Methane}$), measured at 700 °C, confirm that under the proposed conditions of analysis, the GDC5 oxide, displays the best selectivity level towards the production of syngas.

Table 4: Steam methane conversion tests and product distribution on reaction oxidation over GDC5 catalysts at 700 °C and GHSV = 18000 h^{-1}.

Test	$X_{Methane}$ (%)	H_2/CO	S_{CO}	S_{H2}
NDC5	63.7	3.00	97.4	99.5
SDC5	55.2	2.17	94.0	94.0
EDC5	58.7	2.87	95.0	94.3
GDC5	69.3	3.04	98.7	99.4
DDC5	58.2	2.90	95.4	94.0
HDC5	60.1	2.91	97.3	98.5

According to Xiaojing *et. al.* [33] the CO conversion and the H_2 production, increases with temperature, showing a high activity under present reaction conditions, in which the CO and H_2 oxidation reaction is considered as a surface process and the activity is closely linked with oxygen vacancies that enabled the adsorption of the reactant molecules and enhanced the dissociation of oxygen molecules. Under the previous considerations, it is clear that results derived from TPR analysis, confirm that GDC5 oxide is a very active phase towards formation of oxygen vacancies which are the mainly responsibles for the better performance in oxidation reaction. The methane conversion reached by GDC5 sample at 700 °C as has been reported previously [34-36], with excellent results and a strong dependence of active species at higher temperatures. So, lattice oxygen species can migrate from the bulk material to surface and participate of the reforming reaction while the consumed oxygen is replaced continuously by the gaseous phase on the TPB limits, allowing the stimulation of the catalytic activity of all tested samples as has been reported previously [37].

To verify the stability of the GDC5 sample, the steam methane reaction was performed during 10 days under similar reaction conditions. Results are displayed in Fig. 11. Initially, the oxide displays a slight deactivation signal with time after 240 hours on stream, decreasing progressively until 65% on methane conversion, while carbon monoxide and hydrogen selectivity, change about 6% and 8% respectively with respect to initial values. After 100 hours on stream, methane conversion and the selectivities was stabilized, indeed, these results evidence that conditions need to be improved to preserve an optimum reaction under present reaction conditions.

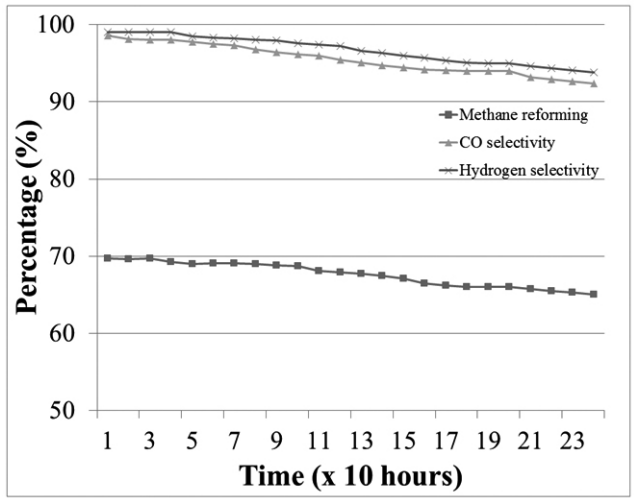

Fig. 11 Stability test during 240 hours for steam methane reaction using GDC5 oxide.

3.4 Post-reaction analysis

The post-reaction analyses of GDC5 sample, suggest no evidence of carbon deposition, according to literature [38, 39], the cerium oxides in a fluorite structure in almost all compositions present a high degree of resistance to carbon deposition after several hours of continuous operation under similar reaction conditions, as shown in scanning and transmission electron micrographs of Fig. 12. Such results are in accordance with previous works [33], in which there is no evidence of carbon deposits or modification in the chemical composition, discarding presence of secondary phases as shown in the XRD analysis of Fig.13 after catalytic test. However it is obvious that a strong sintering phenomenon has occurred, which may lead to premature deactivation of the oxide by loss of the specific area and the crystal growth of the active catalyst phase [40].

Although the kinetics of catalyst deactivation of GDC5 oxide clearly is due to grain sinterization and it depends largely on the temperature, the exposure time and the nature of the reducing atmosphere among other factors, the severe changes in the catalytic activity may be produced by a complementary process that occurs on surface of the oxide, such as reverse water gas shift reaction (RWGS), which is mildly exothermic and can occur rapidly in presence of metallic catalysts at temperatures above 400 °C as shown in Eq. 4 [41].

$$CO_2 + H_2 \rightarrow CO + H_2O + \Delta H = 9.0 \text{ kcal/mol} \qquad (4)$$

Proposed mechanisms confirm that a steam reforming reaction on

multicomponent oxides produces a redox mechanism, where the CO is adsorbed on active sites and reacts with adsorbed oxygen to form CO_2. In next step, the reduced support is subsequently re-oxidized by water vapor, increasing hydrogen concentration and allowing the formation of intermediate species by an associative mechanism, the main reaction is governed by a bidentate intermediate produced by the reaction of CO with terminal hydroxyls on the oxide support, which is decomposed to form H_2 and carbonate species [41, 42]. In this context, although the focus on the study of this type of materials has focused on platinum-based catalysts, it has been found that in most cases and oxides there is a tendency toward the catalyst deactivation by the high concentration of carbon monoxide, while the exposure to high concentrations of CO_2, CH_4, or H_2 leads to a moderate deactivation [43]. This effect can be studied more clearly using complementary characterization techniques as impedance spectroscopy to display the behavior of the material under steady stationary conditions.

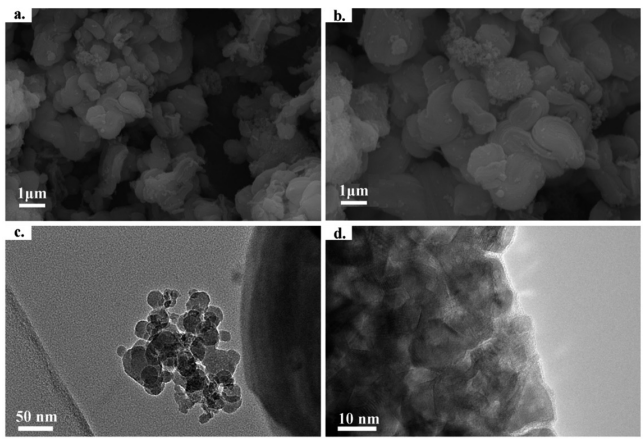

Fig. 12 Scanning (a, b) and transmission (c, d) electron micrographs for the GDC5 oxide after catalytic test.

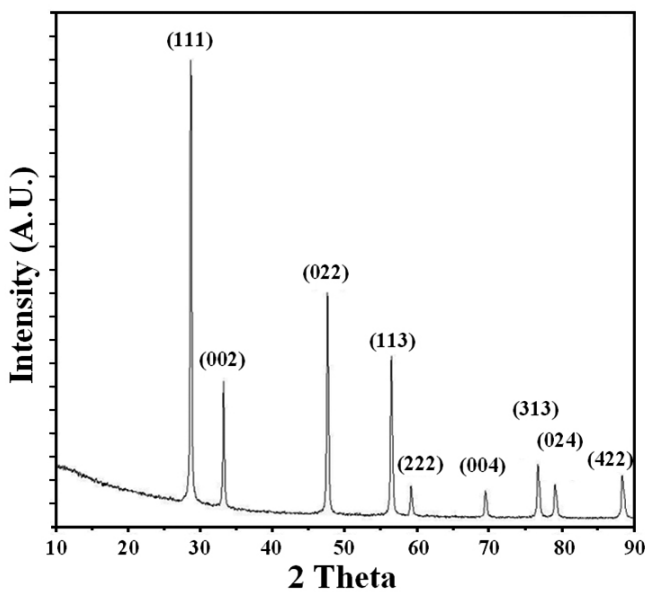

Fig. 13 Diffraction pattern of the GDC5 oxide after 240 hours on stream.

4. CONCLUSIONS

Current method to prepare the 18 oxides based on the system $Ce_{1-x}Ln_xO_{2-\delta}$ (Ln: Nd^{3+}, Sm^{3+}, Eu^{3+}, Gd^{3+}, Dy^{3+} and Ho^{3+}), with x = 0.05, 0.10 and 0.15 mol%, shows a strong correlation with obtention of highly dispersed catalysts, confirming that is possible to obtain nanometric materials by use of a wet chemical route, based on the synthesis of intermediate citrate coordination compounds with active phases toward steam methane reforming reaction.

The physicochemical analyses, confirms the obtention of pure oxides with a heterogeneous appearance due to used synthesis method. The X-ray diffraction and electron microscopy techniques, confirmed presence of nanometric crystallites preferentially oriented in the (1 1 1) facet, with a single crystallographic phase and optimal catalytic properties and selectivity levels to syngas production.

The TPR-H_2 analyses, showed the way in which strong reducing atmospheres, can affect the catalysts under continuous reaction conditions, with these results, were possible to identify the best reaction conditions with purpose to provide a good stability conditions of catalytic test under potential reaction conditions of a SOFC device. At microscopic level and based on the SEM-TEM results, the solids were composed by irregular aggregates with sizes between 0.5 to 150 mm and crystallites sizes between 32 and 47 nm, in which there is no difference between materials with variable degrees of modification, nor there significant changes in the sequence of proposed lanthanide series.

The conductivities of the cerium oxides show different values, with Nd, Gd and Ho as the materials with the highest values. The maximum conductivity observed was 7.57×10^{-7} S cm^{-1} for GDC5 sample in contrast with the SDC5 and DDC5 samples, in which conductivity values reach 1.12×10^{-7} and 1.56×10^{-7} S cm^{-1} respectively. These results vary substantially along substitution series of rare earth oxides, which allowed evaluating the best candidates for tests of steam methane reforming reaction.

All metal oxide catalysts were studied on the steam methane reforming reaction during 6 hours under isothermal reaction at 700 ºC with methane conversion of 69.3% and optimal selectivities to carbon monoxide and hydrogen of 98.7 and 99.4 % respectively for the best catalyst of GDC5; all products were identified by gas chromatography, which permitting us to know some relevant aspects of the catalytic test and its principal products. So, we conclude that formation of different byproducts during reaction time such as CO, CO_2, H_2O, CH_4 and H_2 at high concentration levels, leads to a moderate deactivation of all synthesized oxides.

In situ analyses of the most promissory catalyst of GDC5, permit us to compare and evaluate the effect of continuous reaction for at least 240 hours on stream, the main results confirm a sinterization phenomenon which is responsible for the reduction in methane reforming and the selectivity toward hydrogen and carbon monoxide, however the reduction in these values is in accordance with the current state for these oxidic materials with fluorite structure. Finally with these results was possible to identify some important strategies for synthesis of catalytic oxides with pure phases and high activity to steam methane reforming reaction for potential applications in SOFC technology.

REFERENCES

1. H. L. Chum, R. P. Overend. Fuel Process. Technol. **71,** 187, (2001)
2. S. H. Chan, O. L. Ding. Int. J. Hydrogen. Energ. **30(2)**, 167, (2005)
3. R. J. Gorte, J. M. Vohs. J. Catal. **216(1-2)**, 477, (2003)
4. M. V. Sandoval, A. Matta, T. Matencio, R. Zacarias, G. A. Ludwig, M. A. Korb, C. F Malfatti, P. Gauthier-Maradei, G. H. Gauthier. Solid State Ionics. **261**, 36, (2014)
5. R. Martínez-Coronado, J. A. Alonso, M. T. Fernández-Díaz. J. Power Sources. **258**, 76, (2014)
6. Y. Sun, N. Yan, J. Li, H. Wu, J. L. Luo, K. T. Chuang. Sustainable Energy Technologies and Assessments. **8**, 92, (2014)
7. P. S. Roy, N. K. Park, K. Kim. Int. J. Hydrogen Energy. **39(9)**, 4299, (2014)
8. T. Saradha, A. Subramania, K. Balakrishnan, S. Muzhumathi. Materials Research Bulletin. **68**, 320, (2015)
9. A. Vita, G. Cristiano, C. Italiano, L. Pino, S. Specchia. Applied Catalysis B: Environmental. **162**, 551, (2015)
10. V. Menon, A. Banerjee, J. Dailly, O. Deutschmann. Applied Energy. **149**, 161, (2015)
11. S. D. Angeli, G. Monteleone, A. Giaconia, A. A. Lemonidou. International Journal of Hydrogen Energy. **39(5)**, 1979, (2014).
12. S. Shao, A. W. Shi, C. L. Liu, R. Z. Yang, W. S. Dong. Fuel Processing Technology. **125**, 1, (2014)
13. S. W. Yu, H. H. Huang, C. W. Tang, C. B. Wang. International Journal of Hydrogen Energy. **39(**35), 20700, (2014)

14. W. Wattanathana, N. Nootsuwan, C. Veranitisagul, N. Koonsaeng, N. Laosiripojana, A. Laobuthee. J. Molecular Structure. **1089**, 9, (2015)
15. G. Jacobs, U. M. Graham, E. Chen, P. M. Patterson, A. Dozier, B. H. Davis. J. Catal. **229**, 499, (2005)
16. J. A. Gómez-Cuaspud, M. Schmal. Int. J. Hydrogen Energy. **38**, 7458, (2013)
17. T. P. Yadav, O. N. Srivastava. Ceramics International. **38(7)**, 5783, (2012)
18. V. Morris, P. G. Fleming, J. D. Holmes, M. A. Morris. Chemical Engineering Science. **91**, 102, (2013)
19. K. C. Anjaneya, G. P. Nayaka, J. Manjann, V. M. Ashwin Kumar, G. Govindaraj, K. N. Ganesha. J. Alloys and Compounds. **598**, 33, (2014).
20. M. Lipińska-Chwałek, F. Schulze-Küppers, J. Malzbender. J. European Ceramic Society. **35(5)**, 1539, (2015)
21. C. Bueno-Ferrer, S. Parres-Esclapez, D. Lozano-Castelló, A. Bueno-López. J. Rare Earths. **28(5)**, 647, (2010)
22. S. McIntosh, J. M. Vohs, R. J. Gorte. Electrochim. Acta. **47**, 3815, (2002)
23. M. C. Göbel, G. Gregori, J. Maier. Solid State Ionics. **215**, 45, (2012)
24. K. C. Anjaneya, G. P. Nayaka, J. Manjann, V. M. Ashwin Kumar, G. Govindaraj, K. N. Ganesha. J. Alloys and Compounds. **598**, 33, (2014)
25. P. Gao, Z. Wang, W. F. Z. Liao, K. Liu, W. Wang, X. Bai, E. Wang. Micron. **41(4)**, 301, (2010)
26. T. H. Hsieh, D. T. Ray, Y. P. Fu. Ceramics International. **39**, 7967, (2013)
27. J. X. Zhu, D. F. Zhou, S. R. Guo, J. F Ye, X. F. Hao, X. Q. Cao, J. Meng. J. Power Sources. **174**, 114, (2007)
28. J. Wright, A. V. Virkar. J. Power Sources. **196**, 6118, (2011)
29. I. E. L. Stephens, J. A. Kilner. Solid State Ionics. **177**, 669, (2006)
30. A. Kaddouri, B. Béguin. Catalysis Communications. **46**, 22, (2014)
31. G. Sierra-Gallego, C. Batiot-Dupeyrat, J. Barrault, F. Mondragón. Rev. Fac. Ing. Univ. Antioquia. **44**, 7, (2008)
32. R. M. De Almeida, H. V. Fajardo, D. Z. Mezalira, G. B. Nuernberg, L. K. Noda, L. F. Probst, N. L. V. Carreño. J. Mol. Catal. A: Chem. **259**, 328, (2006)
33. Z. Xiaojing, L. Huaju, L. Yong, S. Wenjie. Chin. J. Catal. **33**, 1109, (2012)
34. S. H. Chan, O. L. Ding. Int. J. Hydrogen. Energ. **30 (2)**: 167, (2005)
35. R. Peters, R. Dahl, U. Klüttgen, C. Palm, D. Stölten. J. Power Sources. **106,** 238, (2002)
36. J. B. Wang, J. C. Jang, T. J. Huang. J. Power Sources. **122**, 122, (2003)
37. Y. Yan, S. C. Sandu, J. Conde, P. Muralt. J. Power Sources. **206**, 84, (2012)
38. J. Ayawanna, D. Wattanasiriwech, S. Wattanasiriwech, K. Sato. Energy Procedia. **34**, 439, (2013)
39. T. J. Huang, J. F. Li. J. Power Sources. **173(**2), 959, (2007)
40. C. H. Bartholomew. Appl. Catal. A: Gen. **212**, 17, (2001)
41. E. P. Fraccari, O. D'Alessandro, J. Sambeth, G. Baronetti, F. Mariño. Fuel Processing Technology. **119**, 67, (2014)
42. D. R. Mullins. Surface Science Reports. **70(1)**, 42, (2015)
43. L. Gradisher, B. Dutcher, M. Fan. Applied Energy. **139**, 335, (2015)